Dynamic NMR Microscopy of Chromatographic Columns

Ulrich Tallarek and Ernst Bayer
Institute of Organic Chemistry, University of Tübingen, D-72076 Tübingen, Germany

Dagmar van Dusschoten, Tom Scheenen, and Henk Van As
Dept. of Molecular Physics, Wageningen Agricultural University and Wageningen NMR Center, 6703 HA Wageningen, The Netherlands

Georges Guiochon
Dept. of Chemistry, University of Tennessee, Knoxville, TN 37996
Chemical and Analytical Sciences Div., Oak Ridge National Laboratory, Oak Ridge, TN 37831

Uwe D. Neue
Waters Corporation, Milford, MA 01757

Pulsed magnetic field gradients encoded a discrete spatial and temporal motion of the molecules of a fluid percolating through the packed bed of a dynamic radial compression column for liquid chromatography. Two packing materials of porous, chemically bonded C18 silica were used: large irregularly shaped particles (55–105 μm) and small spherical particles (6 μm). By combining pulsed field gradient NMR and NMR imaging the distribution of the fluid dynamic displacement probability was determined quantitatively at each point of the static image space. The local axial dispersion coefficient, fluid velocity, and external porosity of the bed were also estimated. The resolution achieved was 250 μm × 250 μm × 2,500 μm per voxel, corresponding to a 250 μm × 250 μm pixel in a 2.5-mm-thick slice. Irregularly shaped particles showed slight external porosity heterogeneities over the column cross section, causing a dramatic loss of performance. Spherically shaped particles offered a nearly planar distribution of the transport characteristics across the packed bed, making radial compression of the bed enhance the performance.

Introduction

The rapid development of the fine-chemical industry and the growing pressure of regulatory demands on the pharmaceutical and biotechnology industries over the last few years have led to a considerable extension of the use of preparative chromatography as a general-purpose separation process in these industries (Guiochon et al., 1994). Among the critical problems that need to be addressed in the scale-up of chromatographic separations are the preparation of large-diameter columns having a separation power comparable to that of analytical columns and a long-term stability. This requires a high degree of homogeneity of the packed bed.

In general, however, column beds have been shown to be inhomogeneous, compressible, and unstable (Guiochon et al., 1997). Column beds are made by pumping a slurry of the packing material into the column and consolidating this slurry progressively. During the preparation of the column and often during the first stages of column operation, a progressive consolidation of the bed takes place. The overall packing density of the bed increases, while its average external porosity and permeability decrease. Static or dynamic bed compression are used to prevent the buildup of large voids that would adversely affect column efficiency due to eddy convec-

Correspondence concerning this article should be addressed to G. Guichon.
Current address of U. Tallarek: Dept. Of Biomolecular Sciences, Laboratory of Molecular Physics, Wageningen Argricultural University and Wageningen NMR Center, 6703 HA Wageningen, The Netherlands.

tion in these voids. Consolidation is achieved under either the viscous stress caused by a high flow velocity of a percolating solvent or an external mechanical compression stress. The former method is used for analytical columns [0.5 in. ID (13 mm) or less]. Better results are obtained with the latter method for the packing of preparative columns. Compression can be implemented in the annular (Lawing et al., 1992), the axial (Godbille and Devaux, 1976), or the radial mode (Little et al., 1976). In all cases, the importance of achieving near plug flow through the column has been stressed (Colin et al., 1990; Yun and Guiochon, 1996; Guiochon et al., 1997). Because the local stress applied during the preparation of the column bed is not constant everywhere, the local density of the packed bed, its external porosity, tortuosity, permeability, and the retention characteristics are not constant but are functions of the radial and axial position (Farkas et al., 1997). As a consequence, the average velocity of solute bands along the individual streampaths in the bed is not constant but is a function of the radial position and the bands are warped during their migration (Farkas et al., 1996, 1997; Farcas and Guiochon, 1997), with nefarious consequences for the separation performance (Yun and Guiochon, 1996).

Giddings (1965) showed that the influence of the fluctuations of the local mobile phase velocity on the column efficiency depends on their spacial scale. He distinguished five different scales and estimated their respective contributions based on a random walk treatment. The role of molecular diffusion is essential in achieving radial homogeneity of the mobile-phase composition through exchange between velocity extremes. While the band broadening itself originates in the velocity inequalities of the flow pattern, the actual extent of the spreading is governed largely by the time- and length-scales of diffusion between fast and slow stream paths. This is why long-term radial fluctuations of the mobile-phase velocity have a much stronger effect than short-term ones. The optimum value of the particle Peclet number (in chromatography the reduced velocity, $\nu = \bar{u}d_p/D_m$ with u mobile-phase velocity, d_p particle size, and D_m molecular diffusivity) for maximum efficiency decreases with increasing bed heterogeneity.

Many authors have clearly demonstrated experimentally the lack of radial homogeneity of chromatographic columns. The main methods used were the recording of chromatograms in different locations in the exit cross-section of the column with microelectrodes and electrochemical detection (Knox et al., 1976; Eon, 1978; Baur et al., 1988; Farkas et al., 1994) or with fiber optics and spectroscopic techniques (Farkas et al., 1996, 1997; Farcas and Guiochon, 1997) to record local band profiles at the column exit. Another approach used the two-dimensional (2-D) and 3-D reconstruction of solute bands during their migration along the column by NMR imaging (Bayer et al., 1989, 1995; Tallarek et al., 1995; Fernandez et al., 1995). The profiles reveal many local irregularities on a general trend that is not planar (Tallarek et al., 1995). Differences between flow velocity distributions observed in dry- and slurry-packed columns seem to be related to the respective packing procedure used to obtain the bed structure (Farkas et al., 1996, 1997). A comparison between the results obtained by the different authors demonstrates the advantage of NMR imaging techniques, which allow the noninvasive visualization of fluid dynamics in opaque systems. These techniques have already been widely used to characterize structural heterogeneities in other porous materials like catalyst support pellets (Hollewand and Gladden, 1995; Gladden et al., 1995), bioreactors (Heath et al., 1990), rocks (Rothwell and Vinegar, 1985; Guilfoyle et al., 1992; Guillot et al., 1994), reservoir cores (Gibbs et al., 1993), soil (Amin et al., 1996; Hemminga and Buurman, 1997), and sludge filter cakes (La Heij et al., 1996).

The heterogeneity of the external porosity of the bed may be responsible for the large differences reported between estimated axial dispersion data and known empirical correlations (Carbonell, 1980; Ahn et al., 1986). Bed heterogeneity may also explain anomalous external mass- or heat-transfer coefficients (Martin, 1978) and can be responsible for biased estimates of the internal diffusivity (Cui et al., 1990). In this respect, Knox and Parcher (1969) have shown that a sharp increase in the height equivalent to a theoretical plate (HETP) is observed for beds having aspect ratios smaller than 8. The radial distributions of the flow velocity depend strongly on the aspect ratio and on the degree of consolidation of the bed. Thus, the similarity between the behavior of narrow (that is, analytical) and wide (that is, preparative and process) packed columns remains questionable.

In this study we use dynamic NMR microscopy (Callaghan et al., 1988; Callaghan, 1993) to measure the spatial distribution of single-phase fluid transport properties in two 25-mm-ID radial compression cartridges, dry- and slurry-packed with large (55–105 μm) and small (6 μm) porous C18 silica particles, respectively. Following this approach, separate maps of dispersion and velocity data can be determined for any thin slice located inside the column, typically provided by 128×128 image matrices with an in-plane resolution of approximately 250 μm and a slice thickness of 2.5 mm. These maps show the radial distribution of the local HETP and porosity and reveal clearly the scale of transport heterogeneities in packed beds which are larger than the voxel (volume element considered in the imaging process) size.

Theory

The most powerful feature of NMR imaging techniques is the variety of contrast mechanisms available (Callaghan, 1993). Depending on the choice of the operator, the signal intensity in an image voxel is controlled by one or a combination of parameters (such as nuclear relaxation times, spin density, or chemical shift separation) that are specifically related to the local structure of the medium observed and the chemical environment. In a packed column, these parameters are directly influenced by the physico-chemical interactions between the chemical groups of the stationary phase and the molecules of the mobile phase and the solute. This allows the recording of images of the packed column or of the eluted solute bands in either a dynamic or a static mode to reveal the structure and homogeneity of the packed bed, the uniformity of the band profile or differences in the degree of wetting (Bayer et al., 1989; Tallerek et al., 1995; Fernandez et al., 1995).

Another contrast mechanism originates from the motion-induced phase shifts in a pulsed field gradient spin-echo (PFGSE) experiment (Callaghan, 1993). In this case, the imposition of imaging (resolution) gradients in a PFGSE NMR

sequence produces motion-dependent phase and amplitude modulation in the acquired image. When combined with high spatial resolution, this method is elegantly suited to a quantitative study of the dynamics of chromatographic columns at the microscopic level since it can image both static and dynamic spin displacements. A Fourier transform of the complex echo signal with its specific modulation due to coherent flow and incoherent dispersion effects (phase and amplitude modulation, respectively) gives the displacement probability distribution of the fluid molecules in each voxel of the porous packing. Depending on the shape and position of this averaged propagator distribution, which are both directly affected by the experimental parameters chosen in a particular experiment (flow rate and observation time scale), it can be utilized to characterize the velocity spectrum of the mobile-phase molecules in a single voxel, the stagnant mobile phase mass-transfer kinetics, the effective axial and transverse diffusion and dispersion, or the local porosity of the packed bed. These voxel-sensitive data can then be collected to derive velocity, dispersion, or porosity maps for a thin slice of the column cross-section.

At this point, it should be noted that the PFGSE NMR motion-encoding technique measures directly the net displacements of the fluid molecules (thus their velocity and dispersion) over a well-defined, but adjustable, experimental observation time Δ, which, in ^{1}H PFGNMR, can range from a few milliseconds up to a few seconds. No tracer molecules need to be introduced into the system as a potential indicator of the underlying fluid-flow field. Consequently, the measurements provide local values of the required fluid dynamics properties averaged over a certain volume of the packing and over a short period of time. By contrast, chromatographic runs necessarily proceed on the scale of the column, last during the whole retention time of the sample injected and usually take several minutes. They require the injection of narrow sample zones at time $t = 0$ and the subsequent acquisition and analysis of the eluted band profile at the column exit, recorded through an on-line detector. Extra-column sources of band broadening found in the injection device, the detector cell, and the connecting tubes are impossible to eliminate and difficult to correct for (Sternberg, 1966). Furthermore, large velocity differences over short distances cause the same bandwidth and bandshape as small differences over large distances (Berdichevsky and Neue, 1990). Thus, if the column is not homogeneous, the average estimates of the column performance obtained from chromatographic methods are difficult to relate to any local property of the column. In this respect, PFGNMR studies can be complemented by an NMR imaging analysis of suitable solute bands (such as Gd(III)-chelates) injected into the column (Bayer et al., 1989; Tallerek et al., 1995). Their migration, broadening, and separation can be followed directly, and the influence of local properties of the column (characterized by dynamic NMR microscopy) on the actual band profile can be properly assigned by comparison with the elution profiles recorded at the column exit with an on-line detector (Tallarek et al., 1995).

The space conjugate to the static displacements $\boldsymbol{r}$ (known as $\boldsymbol{k}$-space) is defined in NMR microscopy by the relation $\boldsymbol{k} = (2\pi)^{-1}\gamma \boldsymbol{G}t$ (Mansfield and Grannell, 1973), where y is the gyromagnetic ratio of the nucleus considered, the vector $\boldsymbol{G}$ denotes the amplitude and direction of the imaging gradient, and t is its duration. In a similar way, the space reciprocal to the dynamic (that is, net) displacement, $\boldsymbol{R} = \boldsymbol{r}' - \boldsymbol{r}$, over an observation time Δ between the successive motion-encoding pulses of magnetic field gradient in PFGSE NMR is known as $\boldsymbol{q}$ space. It is defined by $\boldsymbol{q} = (2\pi)^{-1}\gamma\delta\boldsymbol{g}$, where the vector $\boldsymbol{g}$ stands for the amplitude and direction of the pulsed field gradients which are applied for a short time δ (Callaghan, 1993). In dynamic NMR microscopy, the signal evolution under both the resolution gradient $\boldsymbol{G}$ and the PFGSE gradient $\boldsymbol{g}$ leads to a modulation in both the $\boldsymbol{k}$ and $\boldsymbol{q}$ spaces

$$S(\boldsymbol{k},\boldsymbol{q}) = \int \rho(\boldsymbol{r})\exp[i2\pi\boldsymbol{k}\cdot\boldsymbol{r}]\int \bar{P}(\boldsymbol{R},\Delta)\exp[i2\pi\boldsymbol{q}\cdot\boldsymbol{R}]d\boldsymbol{R}d\boldsymbol{r}$$

$$= \int \rho(\boldsymbol{r})E(\boldsymbol{q},\boldsymbol{r},\Delta)\exp[i2\pi\boldsymbol{k}\cdot\boldsymbol{r}]d\boldsymbol{r} \quad (1)$$

In this equation, $\rho(\boldsymbol{r})$ is the initial spin density in a voxel with coordinate $\boldsymbol{r}$ and $\bar{P}(\boldsymbol{R},\Delta)$ is the displacement probability distribution, the so-called averaged propagator (Kärger and Heink, 1983). This quantity gives the probability that any fluid particle in the voxel (independent of its starting position $\boldsymbol{r}$) undergoes a dynamic displacement $\boldsymbol{R}$ over time Δ along the direction of the applied pulsed magnetic field gradient. Thus, the effect of the PFGSE sequence is to provide contrast $E(\boldsymbol{q},\boldsymbol{r},\Delta)$ to each voxel $\boldsymbol{r}$ in the static image (Callaghan and Xia, 1991) given by

$$E(\boldsymbol{q},\boldsymbol{r},\Delta) = \int \bar{P}(\boldsymbol{R},\Delta)\exp[i2\pi\boldsymbol{q}\cdot\boldsymbol{R}]d\boldsymbol{R} \quad (2)$$

$E(\boldsymbol{q},\boldsymbol{r},\Delta)$ represents the normalized complex echo signal of the voxel in an ideal PFGNMR experiment (that is, one for which $\delta \ll \Delta$ (Stejskal and Tanner, 1965). The intriguing feature of this formalism is that the averaged propagator $\bar{P}(\boldsymbol{R},\Delta)$ can be obtained directly by Fourier transform of $E(\boldsymbol{q},\boldsymbol{r},\Delta)$ with respect to $\boldsymbol{q}$ (Callaghan et al., 1988). At very short observation times, when the path lengths traveled by the fluid molecules are small with respect to the average particle diameter ($\bar{u}\Delta \ll d_p$), the averaged propagator can be analyzed in terms of the probability distribution for the velocity component along the magnetic field gradient and mean flow direction (Lebon et al., 1996). When, by contrast, due to the nature of the convective dispersion process, the correlation between $\boldsymbol{r}'$ and $\boldsymbol{r}$ over time Δ gets completely lost ($\bar{u}\Delta \gg d_p$), the averaged propagator becomes a Gaussian distribution

$$\bar{P}(\boldsymbol{R},\Delta) = \frac{1}{\sqrt{2\pi\sigma^2}}\exp\left[-\frac{(\boldsymbol{R}-\bar{u}\Delta)^2}{2\sigma^2}\right] \quad (3)$$

where $\sigma^2 = 2D_{ap}\Delta$ is the variance, D_{ap} is the apparent dispersion coefficient in the gradient direction, and $\bar{u}$ is the average flow velocity through the voxel cross-section. With this expression for the voxel-averaged displacement probability distribution, $E(\boldsymbol{q},\boldsymbol{r},\Delta)$ becomes an oscillatory function of $\boldsymbol{q}$ (due to the coherent nature of the flow), modulated by a Gaussian decay (due to the incoherent motion of dispersive origin)

$$E(\boldsymbol{q},\boldsymbol{r},\Delta)=\exp\left[-4\pi^2q^2D_{ap}\Delta+i2\pi\boldsymbol{q}\cdot\bar{\boldsymbol{u}}\Delta\right] \quad (4)$$

The complex q-space Fourier transform of this function corresponds to the reconstructed propagator of $E(\boldsymbol{q},\boldsymbol{r},\Delta)$ and is given by the convolution

$$F\{E(\boldsymbol{q},\boldsymbol{r},\Delta)\}=\frac{1}{\sqrt{4\pi D_{ap}\Delta}}\exp\left[-\frac{\boldsymbol{R}^2}{4D_{ap}\Delta}\right]\otimes\delta(\boldsymbol{R}-\bar{\boldsymbol{u}}\Delta) \quad (5)$$

In other words, the distribution of the averaged propagator obtained for each point in the static image space is a Gaussian one, centered at $\bar{u}\Delta$ in the displacement space and having a standard deviation $(2D_{ap}\Delta)^{1/2}$. Thus, the voxel averaged coefficient of apparent dispersion and velocity can be obtained from the width and peak center of the profile, respectively (Figure 1).

Alternately, the dispersion coefficient can be calculated also from the initial attenuation of the voxel echo signal with increasing (but still small) amplitudes of the gradient $\boldsymbol{g}$. In the Fourier sense of Eq. 2, this low-q limit corresponds to the dispersion of the fluid particles experiencing long-range displacements in the column bed. D_{ap} is then derived from the initial slope of the absolute value of $E(\boldsymbol{q},\boldsymbol{r},\Delta)$ plotted vs. q^2, in anticipation of the Gaussian distribution characterizing dispersion in this regime of long-range fluid displacements (Callaghan and Stepisnik, 1996)

$$|E(\boldsymbol{q},\boldsymbol{r},\Delta)|=\exp\left[-4\pi^2q^2D_{ap}\Delta\right] \quad (6)$$

This approach has been used recently to study axial and transverse dispersion in packed beds of chromatographic columns (Tallarek et al., 1996) and in closely related systems (Seymour and Callaghan, 1997). In the present work, we used the PFGNMR technique in combination with NMR imaging spatially to resolve the transport properties (that is, the apparent dispersion and the velocity data) of two chromatographic columns consolidated by radial compression.

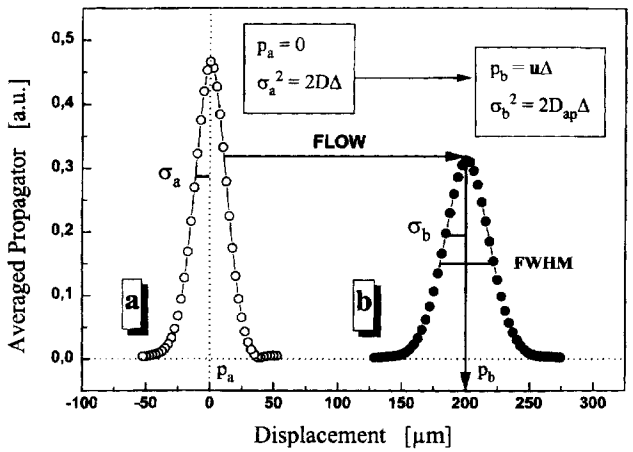

Figure 1. Displacement probability distributions of water molecules recorded with dynamic NMR microscopy in each point of the static image space.

These distributions were obtained in the absence (a) and in the presence (b) of an externally driven convection. The determination of the local molecular diffusivity (D) in the bed, of the apparent axial dispersion (D_{ap}), and of the voxel-averaged velocity ($\bar{u}$) from the respective Gaussian distributions is illustrated (FWHM = full width at half maximum = $2\sigma\sqrt{2\ln 2}$).

Experimental Studies

Liquid chromatography

Studies were performed on two 25×100 mm flexible-walled polyethylene cartridges (Waters, Milford, MA), packed with totally porous, chemically-bonded C18 silica particles. One was dry-packed, using irregularly shaped, large particles (d_p = 55–105 μm, averaged 80 μm). The other one was slurry-packed (Neue, 1997) with spherically shaped Nova-Pak (Waters) particles, having narrow-size distribution around 6 μm. When packed, the 25-mm-ID cartridge was inserted into a custom-built radial compression chamber, made entirely of high tensile strength polymeric materials and designed to operate under a compression pressure of at least 1,000 psi (70 atm). This system allows operation under realistic conditions. A proper system of fittings prevent any fluid from passing from the compression chamber to the stream of mobile-phase percolating through the column or in the opposite direction. The conventional systems used in radial compression chromatography (Biotage, Charlottesville, VA and Waters, Milford, MA) are made of steel, and can operate up to 3,000 psi (210 atm) but are rarely used above 300 psi (21 atm) (Sarker and Guiochon, 1994b). It is obviously impossible to use a steel compression chamber in any NMR investigation. The dry-packed cartridge was wetted with acetonitrile before switching to a stream of pure water as the mobile phase used in the NMR studies. Water was also used as the compression fluid. Prior to their use, the solvents were thoroughly degassed with helium.

Compression of the cartridge was achieved by connecting a conventional HPLC pump (Sykam Model S 1000, Gilching, Germany) directly to the compression chamber using a T-piece. A metering valve allowed easy adjustment of the compression stress. The compression fluid is introduced into the small air gap between the plastic cartridge and cylinder to radially compress the cartridge (Little et al., 1976). The selected compression pressure was set, and the system was monitored through the pressure gauge of the pump. It was adjusted until the compression pressure required for the cartridge and the mobile phase head pressure and flow rate remained constant over time. The backpressure during the measurements carried out with the cartridge packed with 6-μm particles was 20 atm for a flow rate F_v = 30 mL/min of pure water. This is approximately half the constant compression pressure (39 atm). Under these operating conditions, the radial compression column exhibited excellent performance. As shown by Carta and Stringfield (1994) on the basis of a model of radial compression columns that they proposed, the radial compression stress applied should exceed the column back-pressure. This was later confirmed experimentally (Sarker and Guiochon, 1994b; Sarker et al., 1996). Otherwise, the bed, insufficiently compressed, would crack causing a

dramatic loss of column performance. This safety condition was always far exceeded in our experiments.

A second, preparative HPLC pump (Waters Model 4000) was connected to the cartridge. This pump allowed flow rates of mobile phase up to 150 mL/min and column inlet pressures up to 250 atm. The pump was precise and stable. It was placed approximately 1.5 m away from the magnet. Pure, degassed water was continuously pumped through the column under study.

Nuclear magnetic resonance

Measurements were performed at 23 ± 0.5°C on a 0.5-Tesla NMR spectrometer, consisting of a SMIS console (Surrey Medical Imaging Systems, Guildford, U.K.), an iron core magnet (Bruker, Karlsruhe, Germany), an actively shielded gradient probe with a 45-mm-ID air gap, and a solenoidal radio frequency (RF) coil (Doty Scientific, Columbia, OH). In this instrument, the gradient coil system incorporates three orthogonally directed magnetic field gradients. The maximum gradient strengths g_{max} available in the directions parallel and perpendicular to the main magnetic field (the latter coincidental with the average flow direction) are 0.6 and 0.5 T/m, respectively. This value defines the maximum available value of q and limits resolution in the q-space (Callaghan et al., 1991). Data analysis was performed using routines written in-house in IDL (Research Systems Inc., Boulder, CO).

To resolve spatially the transport properties in the packed bed, we have combined PFGSE NMR, used to provide image contrast, with both multiecho (ME) (van Dusschoten et al., 1996) and turbo spin-echo (TSE) imaging (Scheenen et al., 1997). The relative timing of RF and magnetic field gradient pulses for both approaches is shown in Figure 2. In these experiments, the imaging gradients (G_{phase} and G_{read}) provide a probe of the k-space while the PFGSE NMR encoding provides a probe of the q-space. The PFGTSE imaging sequence (Figure 2b) allows complete q-space imaging (that is, the determination of the dynamic displacement distribution profile $\bar{P}(R, \Delta)$ at each point in the static image space) in less than 30 min. However, compared to the pulsed field gradient multiecho (PFGME) imaging sequence (Figure 2a), it is not capable of monitoring simultaneously T_2 (transverse nuclear relaxation time), the fluid density, and the displacement. The additional echos acquired with the PFGME sequence typically were used to enhance the signal-to-noise ratio (SNR).

The radial compression chamber was designed to fit tightly into the 45-mm-ID cylindrical air gap of the gradient system. The setup is shown in Figure 3. The only metallic part is the large screwed cap at the top. It is far enough from the magnet and the column bed not to affect the stability of the magnetic field and the linearity of the field gradient pulses. Most measurements were performed on a thin slice oriented perpendicular to the cartridge axis, containing the complete cylindrical column cross-section, including the compression-chamber (as shown in Figure 3). The 2.5-mm-thick slice selected for the studies was located in the middle of the cartridge, thus eliminating possible column end effects on the results (Knox et al., 1976; Tallarak et al., 1995; Farkas et al., 1997). Slice selection was achieved by a sine-shaped 90° (selective) RF pulse, and the 180° (unselective) RF pulse was substituted by a train of narrow-spaced 180° pulses (Figure 2), generally used to minimize effects due to residual (background) magnetic field gradients in the sample or field instabilities of the magnet (van Dusschoten et al., 1995). However, susceptibility heterogeneities which can affect studies of porous media containing paramagnetic impurities (such as iron) did not constitute a problem in our studies and the (odd) number of 180° pulses was used to adjust the length of the PFGNMR observation time Δ. The packing materials used here contain only traces of paramagnetic impurities, for example, the Fe^{3+} contamination is typically below 10 ppm.

Using repetition times of 1.5 s between succeeding signal averages and taking 4–16 averages, the resulting measurement times for q-space imaging were about 8 h using the PFGME sequence, and approximately 2 h (or less) for the PFGTSE sequence. The field of view (FOV) was 33.02 mm. The images were acquired with a 128×128 pixel matrix and 32 q-steps in the range of $\pm q_{max}$. Prior to applying the Fourier transform, the q data were zerofilled to 64 points (zerofilling consists of adding zeros to the wavevector-domain data set in order to increase the digital resolution of the discrete displacement spectrum resulting from subsequent Fourier transform (Marshall and Verdun, 1990); this procedure is equivalent to data interpolation in the displacement space). In the case of the dispersion data derived from the low-q limit [with $4\pi^2 q^2 D_{ap} \Delta \ll 1$ (Tallarek et al., 1996; Seymour and Callaghan, 1997) cf. Eq. 6], the attenuation of $E(q, r, \Delta)$ was kept below 25%. However, to obtain the complete displacement probability distribution $\bar{P}(R, \Delta)$ the signal was attenuated well into the noise (by proper choice of $\pm q_{max}$) to avoid truncation of the NMR signal at $\pm q_{max}$ and the consecutive effects occurring when doing the Fourier transform of $E(q, r, \Delta)$ with respect to q.

Results and Discussion

The availability of spatially resolved transport properties in packed beds should provide an improved understanding of the relationships between the factors controlling the packing operation of a chromatographic column and its column performance, characterized by the apparent mass-transfer kinetics and the column efficiency, as well as by the resolution of solute bands achieved in chromatographic separations. This understanding requires the intermediate determination of the distributions of the local values of the packing density of the bed, its external porosity, and tortuosity, and permeability of both the mobile-phase velocity and of the axial and the transverse dispersion coefficients.

Figure 4a shows the axial dispersion map obtained for a cartridge packed with 55–105-μm porous C18 silica. The water flow rate through the column is $F_v = 45$ mL/min. The 2.5-mm-thick slice is oriented perpendicularly to the column axis. The contrast in each pixel is given by the voxel-averaged axial dispersion coefficient of water. The cartridge is under radial compression stress, with the pressure in the compression chamber being 36 atm. The brighter the pixel color in the image, the higher the value of the axial dispersion coefficient of water. The water in this chamber is seen as the purple outer ring between the black walls of the cartridge and the compression chamber. This color corresponds to the molecular diffusivity of pure, stationary water, $D_m = 2.15 \times 10^{-9}$ m^2/s at 23°C. Within the cartridge, there are two re-

gions (shown in orange-red) of slightly higher packing density than average (in yellow). In these regions, the flow velocity is markedly lower (see below), which is consistent with the lower axial dispersion coefficients in these regions (as seen in the image). Spin density images, taken separately and in the absence of flow, reveal that the water density in these two clearly visible regions (orange-red) is only slightly lower than average (less than 5%). This fluctuation is most probably caused by a higher packing density, resulting in a reduced value of the local external porosity and of the permeability.

The radial variation of the axial dispersion coefficient along a diameter of the slice of bed studied is shown in Figure 4b. This line goes through the center of one of the critical regions and touches the other one (Figure 4b). Whereas the average dispersion coefficient in the column cross-section is around 1×10^{-7} m^2/s, it is only 2.5×10^{-8} m^2/s in the center

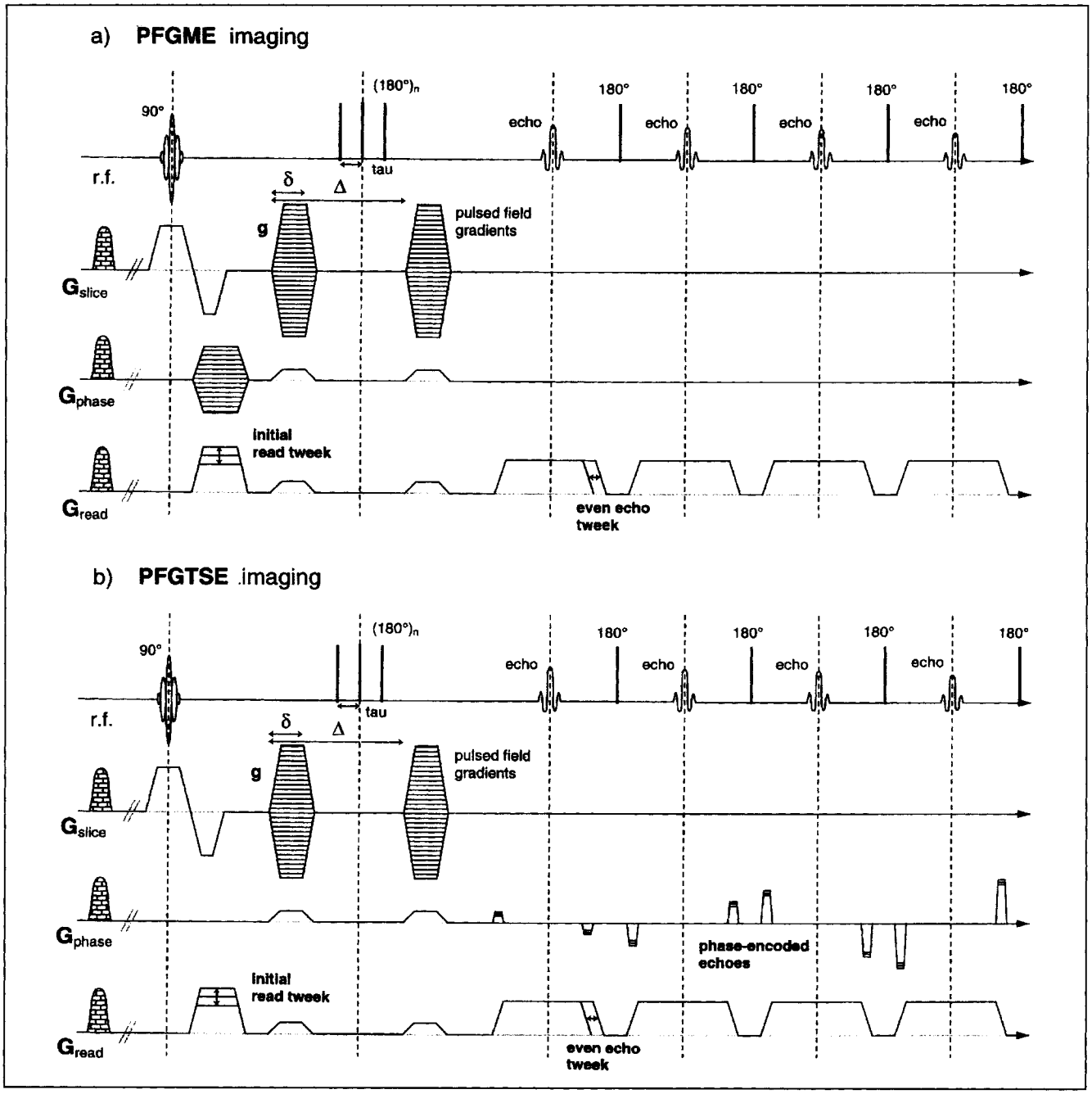

Figure 2. (a) PFGME and (b) PFGTSE sequences used in this dynamic NMR microscopy study.

The selective initial 90° RF pulse excites a rectangular layer of spins normal to the axis of the simultaneously applied slice selection gradient (G_{slice}). The phase-encoding (G_{phase}) and read-out gradient (G_{read}) are used to spatially assign the PFGNMR (propagator) information. This contrast scheme is provided by the embedded pair of pulsed magnetic field gradients (of amplitude g and duration δ), separated in time by Δ. In this work, they are applied in the same direction as the slice selection gradient, that is, along the cartridge axis which is the direction of net flow.

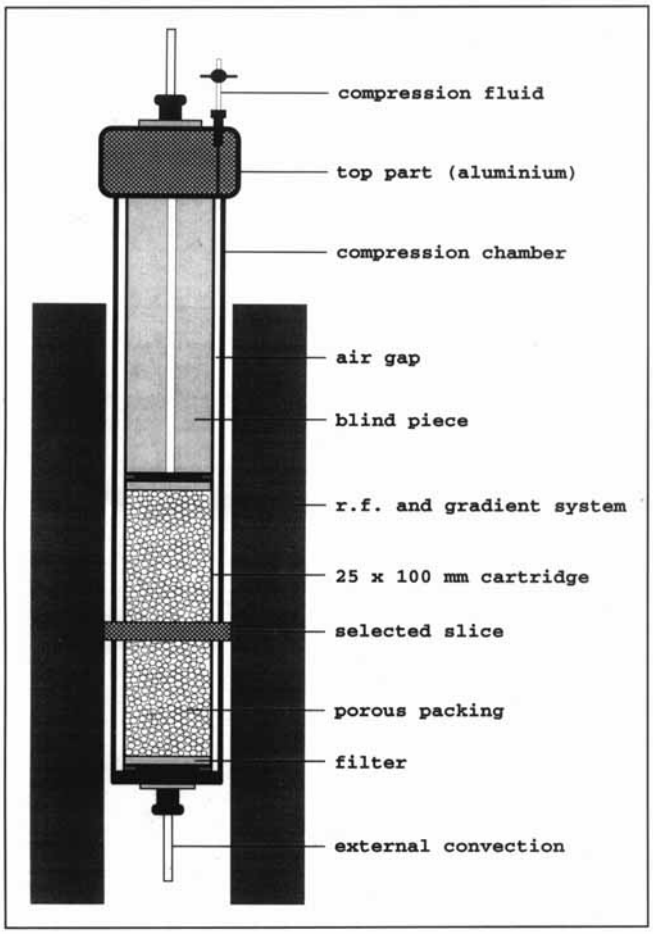

Figure 3. NMR-adapted setup for a radial-compression chromatography column.

The setup is shown adjusted within the RF and gradient coil assembly (itself placed in the center of the magnet). The fluid-phase flow direction is from the bottom to the top of the cartridge.

of the first critical region and about 6×10^{-8} m^2/s in the periphery of the other one (Figure 4b). Note that, since the cartridge is 25 mm in ID and the slice is 2.5 mm thick, the bed and transport heterogeneities occur on a scale of several millimeters. The observation time in this experiment is $\Delta =$ 59.2 ms. Thus, based solely on the diffusivity of water, molecules can diffuse over a distance of only $\sqrt{D_m\Delta} \cong 11$ μm. This is a small fraction of the average particle diameter (≈ 80 μm), barely sufficient to allow a relaxation of the displacement heterogeneities in $\bar{u}\Delta$ by radial dispersion, that is, by convection-driven dispersion assisted by the diffusional exchange of fluid molecules between neighbor streamlines of different velocities. The information obtained on the spacial distribution of the porosity and of the transport heterogeneities in packed beds is of great importance to understand better the band shape and bandwidth of chromatograms recorded on the bulk eluent at the column exit. Irregularities of the flow pattern cause band broadening, the actual extent of which is largely governed by diffusion between the fast and slow stream paths (Giddings, 1965). For the heterogeneities seen in Figure 4a, this requires mass transfer by radial dispersion on a scale of 20 and more particle diameters. In actual chromatographic practice for a given length scale of the velocity inequalities in the porous packing, the displacement heterogeneity induced over a time Δ, together with the radial concentration gradients thus created, becomes most important for solute bands of highly concentrated macromolecules. In this case, the mass transfer in the mobile phase is further limited by the low molecular diffusivity of these compounds.

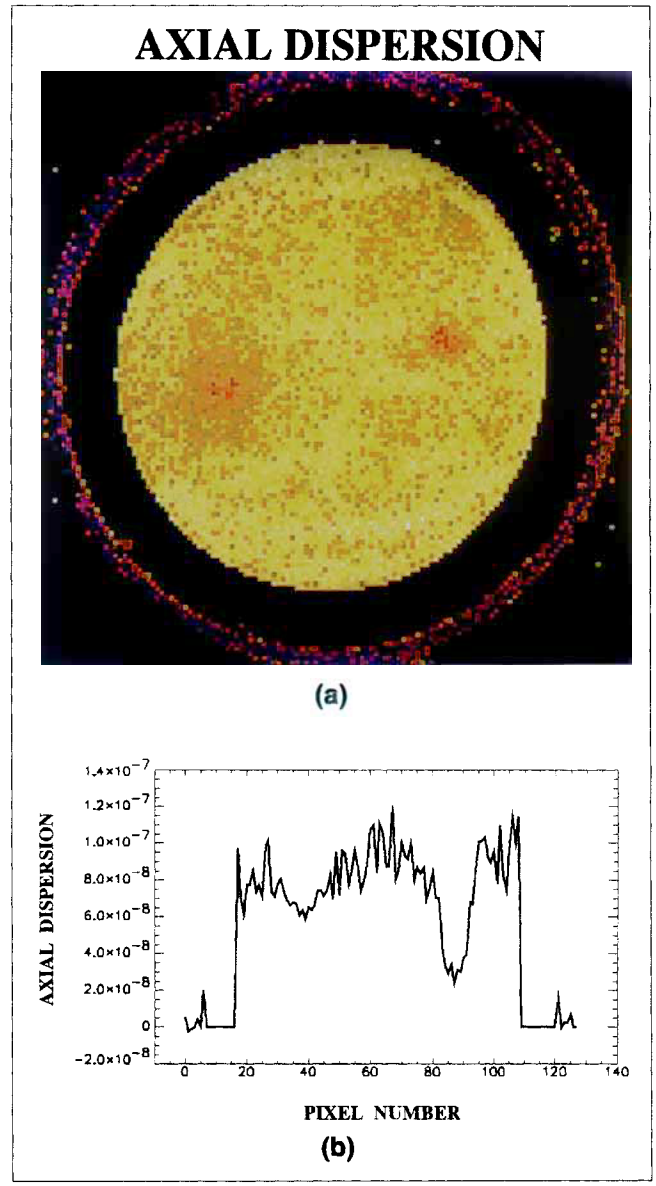

Figure 4. Axial dispersion of water obtained by the PFGME sequence (128 × 128 image matrix).

Flow rate $F_v = 45$ mL/min. Observation time $\Delta = 59.2$ ms. Gradient pulse duration $\delta = 1.5$ ms. The cartridge was packed with irregular-shaped, porous C18 silica particles (with $d_p = 55$–105 μm). (a) Map of the apparent axial dispersion coefficients. The field of view (FOV) is 33.02 mm and the slice thickness 2.5 mm. The coefficient of apparent dispersion is derived from the low-q limit, corresponding to long-range fluid particle displacements in the bed. Outer ring: compression water (36 atm). (b) Plot of the axial dispersion coefficient (D_{ap} [m^2/s]) vs. the radial position (pixel number) in the column cross-section shown in Figure 4a. The data are those from the single pixel row of dimension 250 μm × 2,500 μm × FOV shown in Figure 4a.

The consequences of large-scale heterogeneities in the packing (large with respect to the average size of a single support particle, as those, for example, seen in Figure 4), and of the associated variations of the fluid dynamics are almost impossible to correct for on the scale of the column with dramatic effects on the actual band shape and the resolution of eluted and separated solute bands (Tallarek et al., 1995). The exchange times characteristic for these heterogeneities are simply too long compared to the residence times of the sample bands in the column.

Finally, we observe in Figure 4 that the column bed appears to be homogeneous in the proximity to the wall of the radially compressed cartridge and that no heterogeneities are detected in the wall region. The resolution of 250 μm per pixel corresponds to approximately three particle diameters. It should be large enough to resolve the bed and transport irregularities occurring in this region. It is usually assumed that the wall region is approximately 30–50 particle diameters (Knox et al., 1976; Eon, 1978). While this estimate is in agreement with other data obtained for analytical size columns (Baur et al., 1988; Farkas et al., 1996), recent results have shown it to be wider with larger diameter columns (Farkas et al., 1997a; Farkas and Guiochon, 1997). Unfortunately, no data similar to those acquired on either slurry-packed or axial compression columns are available for radial compression columns at this stage.

In order to obtain quantitative estimates of the displacement spectrum of fluid particles in the regions of interest, the averaged propagator $\bar{P}(\boldsymbol{R}, \Delta)$ was recorded in order to complement the axial dispersion data shown in Figures 4a and 4b. Now, to each individual pixel is associated the complete displacement probability distribution of the fluid molecules in the respective voxel (250 μm $\times$ 250 μm $\times$ 2,500 μm), that is, the spectrum of net traveled (dynamic) distances. Figure 5 compares two such averaged propagator distributions. The first one is taken from the center of the critical region on the righthand side of Figure 4a, where the external porosity is lower than average. The second one is taken from a region close to the column center, where the local properties are representative of the average properties of the bed. In order to increase the SNR, the propagator information was averaged over four pixels, thus covering a total region of 500 μm $\times$ 500 μm $\times$ 2,500 μm, corresponding to a voxel volume of $(850\ \mu\text{m})^3 = 0.6\ \text{mm}^3$.

Based on the water flow rate ($F_v = 45$ mL/min) and the observation time ($\Delta = 84.5$ ms) used in the experiment, a dynamic fluid displacement of $\bar{u}\Delta \approx 0.235 \times 10^{-3}$ m is expected, assuming a total porosity of the bed of the radially compressed cartridge of 0.55 from chromatographic measurements. This value is in agreement with the center position of the displacement probability distribution of the average pixel (curve b in Figure 5). However, the center position of the propagator distribution for the region which has a packing density slightly higher than average (curve a in Figure 5) is much closer to zero and the distribution is more asymmetrical in the flow direction. The curve is similar to the exponentially tailing velocity distribution observed in beds of spherical particles at displacements smaller than the typical interparticle pore size (Lebon et al., 1996; Tessier et al., 1997; Van As et al., 1998). In this case, $\bar{P}(\boldsymbol{R}, \Delta)$ represents the velocity spectrum along the field gradient and net flow direction of the fluid molecules moving along individual channels between the bed particles. As can be inferred from the rounded top of the distribution in Figure 5a and from the population of displacements in the direction opposite to that of the net flow, effects due to molecular diffusion also have to be considered. With increasingly high interstitial fluid velocities, the net distances traveled become larger than the average pore size and the velocity spectrum evolves toward a Gaussian-shaped displacement probability distribution, as seen with curve b in Figure 5 (Tallarek et al., 1998). In this case, the mean displacement (based on the external flow rate and the observation time, $\bar{u}\Delta \approx 0.235 \times 10^{-3}$ m) is three times as large as $d_p = 55$–105 μm. It should be noted, however, that, for both regions in the packed bed, the averaged propagator has not yet achieved the Gaussian shape characteristic of the classical convective dispersion process. In the region with lower external porosity and permeability (Figure 5a), the interstitial velocity is markedly lower than average and $\bar{P}(\boldsymbol{R}, \Delta)$ resembles the distribution of the velocity components of the fluid molecules in the flow direction, while the shape of the propagator distribution characterizing the average cartridge packing properties (Figure 5b) with higher interstitial flow velocities exhibits already a pronounced contribution of dispersive motions.

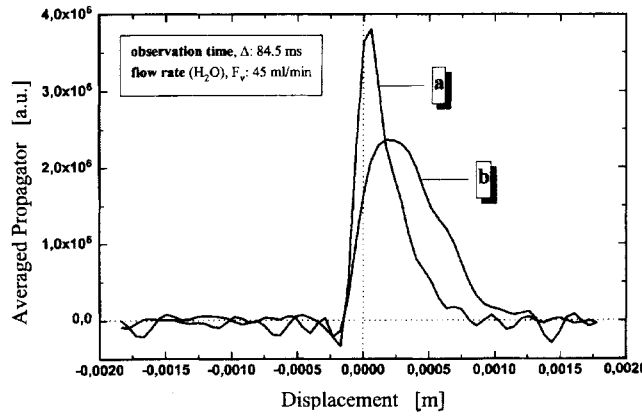

Figure 5. Axial displacement probability distributions for water in selected regions of the column cross section (PFGME sequence; 128 × 128 image matrix and 32 q-steps, zerofilled to 64 points; FOV: 33.02 mm).

The data were averaged over a quadratic array of four pixels (that is, 500 μm × 500 μm) with a slice thickness of 2,500 μm. They correspond to two regions of the column, one where the mobile-phase velocity is abnormally low (a), the other where it is close to average (b). The cartridge was packed with irregular-shaped, porous C18 silica particles (with $d_p = 55$–105 μm).

The heterogeneity of the bed affects the local fluid velocity. At low Reynolds numbers at which inertial effects can be neglected, the local velocity and the local external porosity are related through the Kozeny-Carman equation, which gives the bed permeability K as a function of the external porosity ϵ_e and the average particle diameter (Blake, 1922; Carman, 1937; Bear, 1988)

$$K = \frac{d_p^2}{\kappa} \frac{\epsilon_e^3}{(1-\epsilon_e)^2} \tag{7}$$

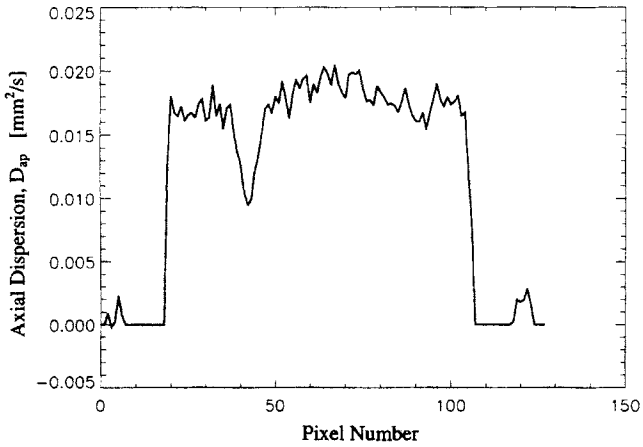

Figure 6. Axial dispersion coefficient (calculated from the low-q limit) vs. radial position, along a diameter of the column slice.

The data are averaged over the two adjacent pixel rows, that is, the line has a thickness of 500 μm and corresponds to a volume of 500 μm × 2,500 μm × FOV (33.02 mm). PFGME sequence is $\Delta = 9.6$ ms, $\delta = 3.0$ ms. Flow rate, F_v: 75 mL/min. Compression pressure: 36 atm. The cartridge was packed with irregular-shaped, porous C18 silica particles (with $d_p = 55$–105 μm).

where K is the Kozeny constant, a function of the porosity and particle shape (Bear, 1988), which is often assumed to be equal to 180. We assume that the local parameters follow the same relationship as the average ones for which the correlation has been derived. Equation 7 demonstrates the extreme sensitivity of the dependence of the bed permeability on the external porosity ($\propto \epsilon_e^5$). Fluctuations of the porosity also affect the local retention factor, although to a lesser degree than the flow rate. The retention factor is proportional to the local density of the stationary phase $(1-\epsilon_e)/\rho_a$ with ρ_a the apparent density of adsorbent particles. The observations so far clearly underline the importance of Eq. 7.

It should be pointed out that when the first measurements were made on the dry-packed cartridge containing the irregularly shaped 55–105 μm porous C18 silica particles, only one of the two regions of low external porosity was observed, the one on the righthand side of the column cross-section shown in Figure 4a. The first plot of the axial dispersion coefficient along the column diameter going through the center of this region is given in Figure 6. It is similar to the one shown in Figure 4b, but the same diameter is oriented in the opposite direction. When the radially compressed cartridge was introduced in the magnet the second time for the acquisition of the data described in Figures 4 and 5, its axial orientation was different and it happened that the two scans of voxel-averaged dispersion data were made in opposite directions with respect to the region of lower external porosity. However, the axial position of the column was strictly controlled, so the data do pertain to the same slice. Another difference between the data reported in Figures 4b and 6 is that the latter were obtained at a volume flow rate of 75 mL/min and with a short observation time ($\Delta = 9.6$ ms). In this case, the high average interstitial fluid velocity combined with the short observation time was selected to impart a strong displacement heterogeneity for the fluid molecules traversing regions of different external porosity and permeability. The short observation time ensures that the contribution of convective displacements (including convective or eddy dispersion) strongly exceeds that of molecular diffusion. The flow rate corresponds to a particle Peclet number of $\nu \sim 250$, assuming an external porosity of 0.36 for the radially compressed bed.

Figure 6 shows that the axial dispersion coefficient in the original critical region is approximately half the cross-sectional average value. This clear and distinct feature is overlaid on an otherwise planar if noisy profile. When the second series of measurements were made (Figures 4a and 4b), a few weeks after the acquisition of the data in Figure 6, the second region of low porosity appeared. The formation of this region was probably a result of the decompression and recompression of the bed and/or of the intermediate storage. In addition, within the first critical region, the one present right from the beginning (Figure 6), the degree of heterogeneity increased, as can be inferred from the further two-fold decrease of the axial dispersion coefficient in the center of this region, relative to the average value in the column cross-section (cf. Figures 4b and 6).

With respect to these observations, it was shown that the external porosity of radially compressed beds decreases with increasing compression stress, while the head pressure required to achieve a certain flow rate increases accordingly (Sarker and Guiochon, 1994a; Sarker et al., 1996). It has been demonstrated by Train (1957) that during the process of pelleting (that is, during compression inside a cylindrical die) the distribution of stress inside the mass of powder is far from uniform throughout the volume of the resulting tablet. Also, compared to particles of almost spherical shape and narrow size-distribution, the beds made of irregularly shaped particles show a different compression behavior. Mechanical compression over a much longer time is needed to reach a constant consolidation state, with the consolidation steps being chaotic in height and time (Fernandez et al., 1995; Sarker et al., 1996). Fragmentation, chipping, and aggregation into lumps were also frequently reported with irregularly shaped particles (Sarker et al., 1996). These observations are complemented by the results on the radial homogeneity and the long-term stability of the compressed cartridge packed with irregularly shaped particles, $d_p = 55$–105 μm shown in Figures 4 to 6, and obtained noninvasively, during column operation, by dynamic NMR microscopy. Similar observations on the correlation between the length scale of the bed heterogeneities and the consolidation of a porous packing were made by Oger et al. (1992) in their study of tracer dispersion by frontal analysis in systems formed from nonconsolidated and fritted, nonporous glass beads of the same initial diameter. For the nonconsolidated beads (porosity 0.37), the studies of Oger et al. revealed a dispersion length l_d of the order of 0.5 d_p (l_d is equal to the Lagrangian correlation length of the flow velocity field). For the fritted glass beads (porosity 0.24), still representing a well interconnected pore network, they found a dispersion length of nearly 30 d_p. Thus, while in the former case the dispersion is uniquely determined by the microscopic structure of the medium, the study demonstrated the existence of structures 30 times larger than the support particle in the fritted glass beads.

The second packing material used in the experiments is made of spherically shaped, porous C18 silica particles, with a narrow particle-size distribution around 6 μm and an aver-

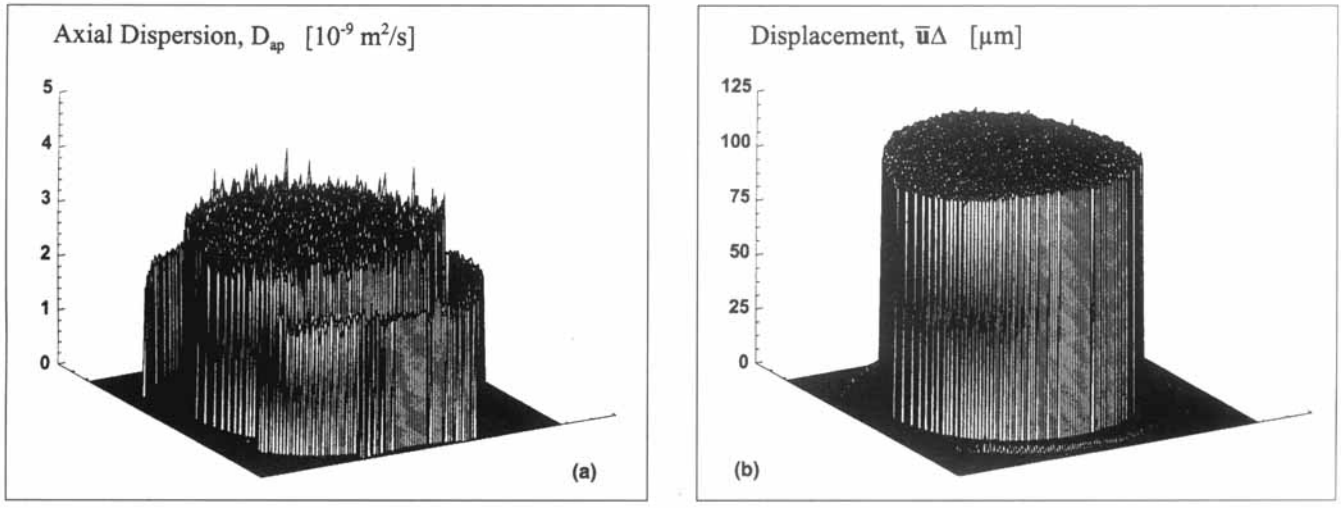

Figure 7. Maps of apparent axial dispersion coefficient (D_{ap}, 10^{-9} m^2/s, Figure 7a) and axial displacement (μm, Figure 7b).

Mobile phase: water. The cartridge was packed with spherical-shaped, porous C18 silica particles (with $d_p = 6$ μm). Slice thickness: 2.5 mm. Flow rate $F_v = 30$ mL/min, radial compression pressure: 39 atm. PFGTSE sequence (128×128 pixel, FOV: 33.02 mm); $\Delta = 64.3$ ms, $\delta = 3.0$ ms.

age internal pore size of 60 Å. The 25×100 mm cartridge was slurry-packed and radially compressed at 38–40 atm. This compression stress was kept constant over the complete duration of the measurement, typically less than 2 h (using the PFGTSE sequence, see the Experimental Studies section). The values of the axial dispersion obtained in the same thin slice, as described in Figure 3 and used in Figures 4 to 6, at a volume flow rate of 30 mL/min, are shown in Figures 7a and 7b. The observation time is $\Delta = 64.3$ ms. The figure demonstrates an almost completely flat distribution of the axial dispersion coefficient (Figure 7a) and of the net fluid particle displacement (Figure 7b), hence of the water velocity, throughout the entire column cross-section. Note, however, that the geometrical dimensions of the pixels have not changed but that the pixel edge corresponds now to 41 particle diameters ($d_p = 6$ μm). As in Figures 4a and 4b, the outer ring is due to the water in the compression chamber. In the axial dispersion map (Figure 7a) it corresponds to the molecular diffusivity of water, whereas in the displacement or velocity map (Figure 7b), it represents still water. This signal can be advantageously used as an internal standard to calibrate the measurements of dispersion coefficients.

The dispersion (D_{ap}) and the dynamic displacement maps ($\bar{u}\Delta$) in Figures 7a and 7b are derived from the averaged propagator information originally obtained for each point in the static image space. This is illustrated in Figures 8a and 8b for the displacement probability distribution of a single voxel (250 μm×250 μm×2,500 μm) with voxel volume of 535 μm^3. Assuming a total porosity of the mobile phase in the bed of 0.55 (see later in the article), this voxel volume (535 μm)^3

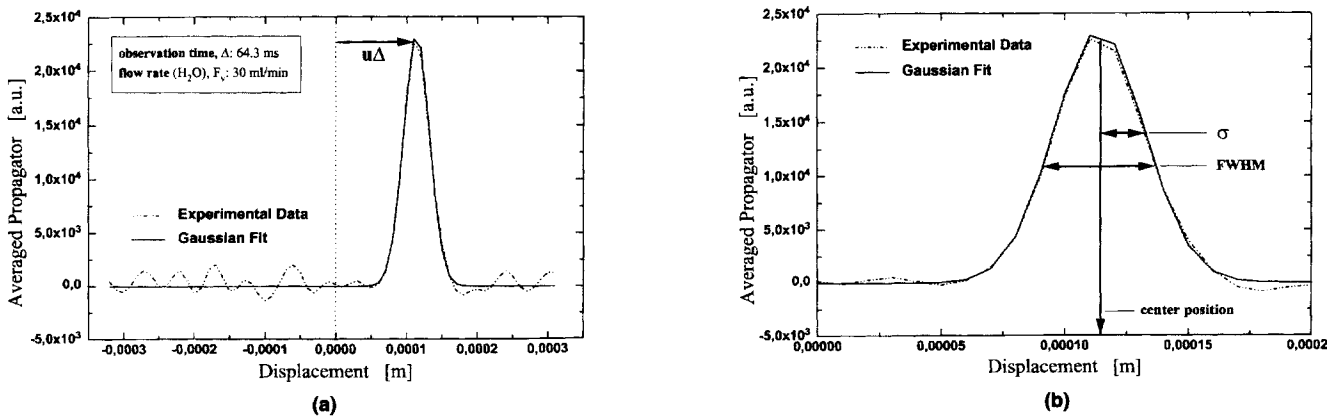

Figure 8. Axial displacement probability distribution for one pixel and best fit to a Gaussian profile.

Same type of plot as shown in Figures 1 and 6. The voxel-averaged fluid velocity ($\bar{u}$) and the apparent axial dispersion coefficient (D_{ap}) were calculated from the profile peak center (at $\bar{u}\Delta$, Figure 8a) and the distribution width (via σ or the FWHM, Figure 8b). The cartridge was packed with spherical-shaped, porous C18 silica particles (with $d_p = 6$ μm).

contains 0.084 mm^3 of water. Figure 8a shows the total propagator information for a representative voxel, obtained from the raw data (acquired in q-space) after zerofilling and Fourier transform with respect to q. Also shown is the best Gaussian fit to the experimental data. The fit of the experimental data for a single voxel is almost perfect. No fluid fraction is found being left at zero net displacement, that is, when the exchange between the stagnant (diffusion-limited) liquid inside the pores of the particles and the fluid percolating the interparticle void space is complete. If this were not the case, due to the choice of a short observation time (or to the use of a packing material with large porous particles), the intraparticle fluid molecules which did not have time to exchange with those in the external volume would show up at a zero net displacement. This allows the study of the mobile-phase mass-transfer resistances in chromatographic columns (Tallarek et al., 1998). Furthermore, compared with what happened with the larger, irregular-shaped particles ($d_p = 55-105$ μm) at similar flow rates and observation times, the dynamic displacements of the fluid molecules have now become much larger than the average particle size ($\bar{u}\Delta \gg d_p$, with $d_p = 6$ μm), so the Gaussian-shaped propagator distribution, characterizing the classic convective dispersion process, is completely developed (Tallarek et al., 1998), a trend that has been indicated earlier in the discussion of the experiments made with the larger particles.

Due to the external convection, the center position of the Gaussian propagator is found at a (net) displacement which depends on the actual observation time (Δ) and the voxel-averaged flow velocity ($\bar{u}$). The latter is related to the particle Peclet number (Pe), or reduced velocity (υ), in that voxel by the classic relationship

$$Pe \equiv \nu = \frac{\bar{u}d_p}{D_m} = \frac{4F_\upsilon d_p}{\epsilon_T \pi d_c^2 D_m} \tag{8}$$

where F_υ denotes the volume flow rate, $4/(\pi d_c^2)$ is the reverse of the column cross-sectional area with d_c the column diameter, and ϵ_T stands for the total porosity of the voxel. Thus, as illustrated in Figure 8b, the propagator distribution contains a wealth of information. First, from the center position of the Gaussian distribution at $\bar{u}\Delta$, the voxel-averaged velocity and porosity can be calculated. Thus, the displacement data shown in Figure 7b also could be expressed in the form of a porosity or a velocity map. For this particular measurement, at $F_\upsilon = 30$ mL/min and $\Delta = 64.3$ ms, we find: $\bar{u}\Delta = 115$ μm (cf. displacement map in Figure 7b); $\bar{u} = 1.79$ mm/s; and $\epsilon_T = 0.56$.

Secondly, from the standard deviation (σ) of the Gaussian distribution, the axial dispersion coefficient can be calculated ($\sigma^2 = 2D_{ap}\Delta$). Here, we obtain: $\sigma = 21.5$ μm; $D_{ap} = 3.65 \times 10^{-9}$ m^2/s (cf. dispersion map in Figure 7a).

The value of the voxel total porosity obtained directly by this original method is typical of the values obtained for radially compressed Nova-Pak cartridges, in agreement with an internal porosity of ca. 30% for the porous Nova-Pak particles and an external porosity of the fully compressed cartridge of approximately 33 to 35%. This would give a total porosity of $0.33 + 0.67 \times 0.30 = 0.53$ to be compared with the measured value of 0.56.

The plug-like character of the flow in the second cartridge is further illustrated in Figures 9a and 9b. The volume flow rate during the experiments reported here was kept constant at $F_\upsilon = 20$ mL/min. In Figure 9a, the observation time was increased in successive steps from $\Delta = 7$ (curve A) up to 64 ms (curve D). The displacement data ($\bar{u}\Delta$) collected along a diameter of the slice studied are plotted vs. the pixel rank. These displacements are similar to those shown in the dynamic displacement map shown in Figure 7b (different values of F_υ and Δ). Figure 9a shows that, as predicted by Eq. 3, a doubling of the observation time results in dynamic fluid displacements which are exactly twice as large, such as for $\Delta = 16$ (curve B) and 64 (curve D) ms, the average net traveled distance is $\bar{u}\Delta = 20$ and 80 μm, respectively. Similarly, Figure 9b demonstrates that the flow rate and the observation time have the same influence on the dynamic displacements of the fluid molecules and are interchangeable. By contrast, the axial dispersion coefficient at a given dynamic displacement

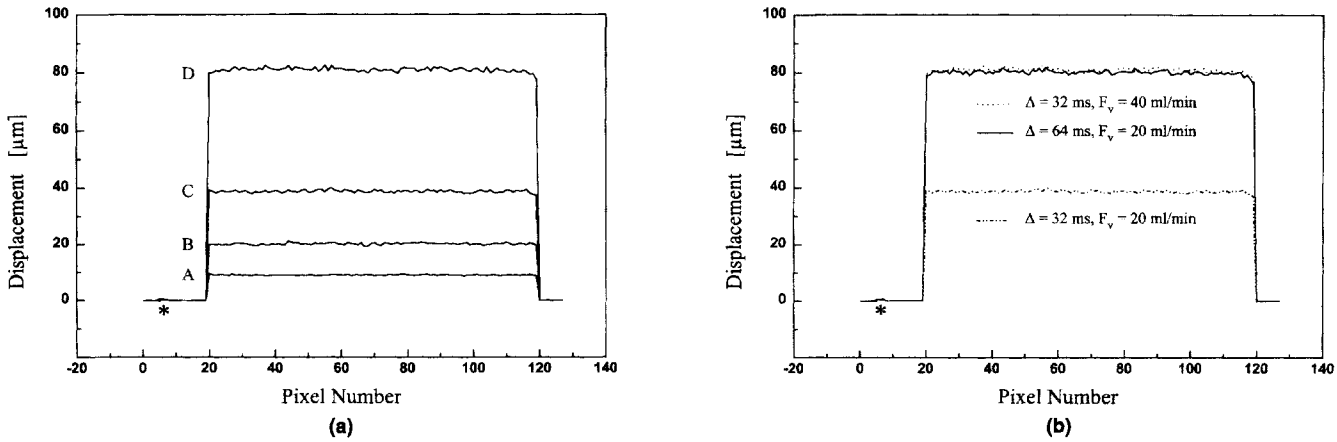

Figure 9. Dynamic displacement ($\bar{u}\Delta$) vs. radial position.

The data were recorded along a single pixel row (250 μm × 2,500 μm × FOV, 33.02 mm). The cartridge was packed with spherical-shaped, porous C18 silica particles (with $d_p = 6$ μm). * denotes the water in the compression chamber ($\bar{u}\Delta \approx 0$). (a) Displacement profiles at constant flow rate ($F_\upsilon = 20$ mL/min), obtained for different observation times: $\Delta = 7$ ms (line A), 16 ms (line B), 32 ms (line C), and 64 ms (line D). (b) Displacement profiles at different combinations of flow rate and observation time, illustrating the exchangeability of the two parameters in $\bar{u}\Delta$.

($\bar{u}\Delta$) depends on the actual Peclet number (through $\bar{u}$) (Tallarek et al., 1996; Seymour and Callaghan, 1997). Then, the two parameters play different roles. The value of Δ controls the extent of the diffusional exchange processes in the packed bed. As these processes take place at different rates on different length scales in the bed (Giddings, 1965), the influence of Δ (via $\sqrt{D_m\Delta}$) is strongly coupled to the actual range of the transport heterogeneities in the packed bed and to the distances covered by the various exchange processes between associated velocity extremes in the mobile phase (Giddings, 1965; Tallarek et al., 1996) as illustrated in Figures 4 and 5. The exchangeability of $\bar{u}$ and Δ regarding the observed distribution of the dynamic displacements across the column demonstrates that, for the slice studied, the distances traveled by the fluid molecules are much larger than the characteristic dispersion length l_d for the fluid flow field, and that Δ is much longer than the correlation time for the velocity fluctuations. In this regime, the dispersion coefficient is found to be independent of the observation time (Seymour and Callaghan, 1997; Van As et al., 1998). The results on the column radial homogeneity obtained respectively with the larger and the smaller particles also indicate the importance of the aspect ratio ($r_a = d_c/d_p$) at constant column length. For the consolidation or the aggregation of particles into lumps, the characteristic dispersion lengths associated with the larger particles ($r_a \simeq 300$) is important on the scale of the column dimension (nearly 10% of the column diameter with $l_d = 25\ d_p$) but is barely so with the small 6 μm particles, for which the aspect ratio is 15 times higher.

The axial dispersion coefficient derived from the displacement probability distributions of the different pixels along a diameter of the slice studied are plotted vs. the pixel rank in Figure 10, for two different flow rates and the same observation time. These data confirm the high degree of homogeneity of the column, illustrated by the flat cross-sectional trend and the comparatively small scatter of the values. They also show that the dispersion coefficient increases with increasing Peclet number. With 6 μm particles, a flow rate of 30 mL/min corresponds to a reduced velocity of approximately 5, a value

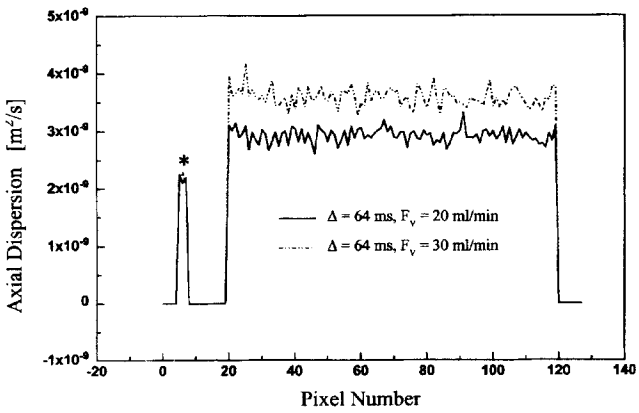

Figure 10. Apparent axial dispersion coefficient (D_{ap}) vs. radial position.

Same origin of the data and same cartridge as for Figures 9a and 9b. PFGTSE sequences; $\Delta = 64$ ms, $\delta = 3.0$ ms. * denotes water in compression chamber (with D_m between 2.1 and 2.4×10^{-9} m^2/s).

which falls in the range of reduced velocities within which liquid chromatography is typically carried out ($3 < Pe < 15$).

The flatness of the radial profiles of the mobile-phase velocities and the coefficients of axial dispersion observed show that the voxel-averaged external porosity distribution is homogeneous and suggests that the same should be true for the voxel-averaged retention factor. This last parameter cannot be measured by the method used here. The motion-encoding PFGSE NMR technique measures directly the fluid dispersion and its average velocity through the bed. Because of the low sensitivity of NMR, a dilute solution of a retained compound in the mobile phase cannot be used in the measurements. Thus, the experimental data presented suggest that this column should give excellent chromatographic performance, insofar as the slice studied is representative of the whole bed. End effects may contribute more to the overall performance than has been assumed so far. Still, the degree of heterogeneity of either the velocity or the dispersion observed with this column on the scale of one or a few pixels is small. Relaxation of concentrations gradients taking place over a distance of 0.25 mm, the pixel size, takes no more than 10 s with a dispersion coefficient of 3×10^{-9} m^2/s (Figure 10). In this case, only the contributions of the transchannel and the short-range interchannel dispersion (Giddings, 1965) to the column efficiency would be significant. Finally, the cartridge was found to remain stable over the several weeks needed for the measurements. No change in the parameters of the displacement distribution were observed at variance with the results obtained with the 55–105 μm irregular particles. The long-term stability of the radially compressed bed is an important factor of its successful performance in industrial applications. The higher performance achieved with the Nova-Pak particles is due to the very characteristics of these particles. However, it is difficult at this stage to sort out the separate influence of their spherical shape (which allows easier relative movements of the particles during consolidation), their narrow-size distribution (which narrows markedly the interparticle pore-size distribution (Karger et al., 1973)), and their lower internal porosity from that of the method used initially to pack the cartridges (that is, dry-packing vs. slurry packing).

Since the pulsed field gradient turbo spin echo (PFGTSE) sequence allows complete q-space imaging in less than 1 h, subsequent slices within the same cartridge could be studied easily. For example, by taking a slice thickness of 1,000 μm, measurements on slices properly spaced would allow a reasonably complete examination of the whole cartridge bed (25 $\times$100 mm) in a few days. This would provide access to the 3-D dynamic anatomy of chromatographic columns (with a voxel dimension of 250 μm$\times$250 μm$\times$1,000 μm), including the acquisition of accurate values of important local properties, that is, the effective diffusion and the bed tortuosity, the axial and transverse dispersion coefficients, the rate coefficient of mass-transfer kinetics between the mobile and the stagnant fluid, the mobile-phase velocity, and the external porosity of the column bed.

Acknowledgment

This work was supported in part by the Human Capital and Mobility Grant ERBCHGECT-940061 of the European Union and by Grant DE-FG05-88ER13859 of the U.S. Dept. of Energy. We thank

Frank Vergeldt (Wageningen Agricultural University) for computational assistance and Yuri Tuvim (Waters Corporation) for the design of the compression chamber.

Notation

$\boldsymbol{k}$ = reciprocal space vector, static image space
$\boldsymbol{q}$ = reciprocal space vector, dynamic displacement space
τ = duration of imaging magnetic field gradient
γ = gyromagnetic ratio of atomic nucleus
ϵ_e = packed beds external porosity
ϵ_T = total porosity
ρ_a = apparent density of adsorbent particles

Literature Cited

Ahn, B. J., A. Zoulalian, and J. M. Smith, "Axial Dispersion in Packed Beds with Large Wall Effect," *AIChE J.*, **32**, 170 (1986).

Amin, M. H. G., K. S. Richards, R. J. Chorley, S. J. Gibbs, T. A. Carpenter, and L. D. Hall, "Study of Soil-Water Transport by MRI," *Magn. Reson. Imaging*, **14**, 879 (1996).

Baur, J. E., E. W. Kristensen, and P. M. Wightman, "Radial Dispersion from Commercial High-Performance Liquid Chromatography Columns Investigated with Microvoltammetric Electrodes," *Anal. Chem.*, **60**, 2334 (1988).

Bayer, E., E. Baumeister, U. Tallarek, K. Albert, and G. Guiochon, "NMR Imaging of the Chromatographic Process. Deposition and Removal of Gadolinium Ions on an RPLC Column," *J. Chromatog. A*, **704**, 37 (1995).

Bayer, E., W. Müller, M. Ilg, and K. Albert, "Visualization of Chromatographic Separations by NMR Imaging," *Angew. Chem. Int. Ed. Engl.*, **28**, 1029 (1989).

Bear, J., *Dynamics of Fluids in Porous Media*, Dover, New York (1988).

Berdichevsky, A. L., and U. D. Neue, "Nature of the Eddy Dispersion in Packed Beds," *J. Chromatog.*, **535**, 189 (1990).

Blake, F. C., "The Resistance of Packing to Fluid Flow," *Trans. Amer. Inst. Chem. Eng.*, **14**, 415 (1922).

Callaghan, P. T., *Principles of Nuclear Magnetic Resonance Microscopy*, Clarendon Press, Oxford (1993).

Callaghan, P. T., A. Coy, D. MacGowan, K. J. Packer, and F. O. Zelaya, "Diffraction-Like Effects in NMR Diffusion Studies of Fluids in Porous Solids," *Nature*, **351**, 467 (1991).

Callaghan, P. T., C. D. Eccles, and Y. Xia, "NMR Microscopy of Dynamic Displacements: k-space and q-space imaging," *J. Phys. E: Sci. Instrum.*, **21**, 820 (1988).

Callaghan, P. T., and J. Stepisnik, "Generalized Analysis of Motion Using Magnetic Field Gradients," *Adv. Opt. Magn. Reson.*, **19**, 325 (1996).

Callaghan, P. T., and Y. Xia, "Velocity and Diffusion Imaging in Dynamic NMR Microscopy," *J. Magn. Reson.*, **91**, 326 (1991).

Carbonell, R. G., "Flow Nonuniformities in Packed Beds: Effects on Dispersion," *Chem. Eng. Sci.*, **35**, 1347 (1980).

Carman, P. C., "Fluid Flow through a Granular Bed," *Trans. Inst. Chem. Eng. (London)*, **15**, 150 (1937).

Carta, G., and W. B. Stringfield, "Operating Characteristics of a Preparative-Scale Radial Compression Chromatograph in Isocratic and Gradient Elution," *J. Chromatog. A*, **658**, 407 (1994).

Colin, H., P. Hilaireau, and J. de Tournemire, "Preparative Liquid Chromatography with a Dynamic Axial Compression Column," *LC-GC*, **3**(4), 40 (1990).

Cui, L. C., D. Schweich, and J. Villermaux, "Consequence of Flow Nonuniformity on the Measurement of Effective Diffusivity," *AIChE J.*, **36**, 86 (1990).

Eon, C. H., "Comparison of Broadening Patterns in Regular and Radially Compressed Large-Diameter Columns," *J. Chromatog.*, **149**, 29 (1978).

Farkas, T., "The Study of Column Packing Homogeneity and Flow Profiles in Packed Chromatographic Columns," PhD Thesis, Univ. of Tennessee, Knoxville (1997).

Farkas, T., J. Q. Chambers, and G. Guiochon, "Column Efficiency and Radial Homogeneity in Liquid Chromatography," *J. Chromatog.*, **679**, 231 (1994).

Farkas, T., M. J. Sepaniak, and G. Guiochon, "Column Radial Homogeneity in HPLC," *J. Chromatog. A*, **740**, 169 (1996).

Farkas, T., M. J. Sepaniak, and G. Guiochon, "Radial Distribution of the Flow Velocity, Efficiency and Concentration in a Wide HPLC Column," *AIChE J.*, **43**, 1964 (1997).

Farkas, T., and G. Guiochon, "Contribution of the Radial Distribution of the Flow Velocity to Band Broadening in HPLC Columns," *Anal. Chem.*, **69**, 4592 (1997).

Fernandez, E. J., C. A. Grotegut, G. W. Braun, K. J. Kirschner, J. R. Staudaher, M. L. Dickson, and V. L. Fernandez, "The Effects of Permeability Heterogeneity on Miscible Viscous Fingering: A Three-Dimensional Magnetic Resonance Imaging Analysis," *Phys. Fluids*, **7**, 468 (1995).

Gibbs, S. J., J. J. Attard, and L. D. Hall, "Diffusion in Brine-Saturated Reservoir Cores Studied by NMR Imaging," *AIChE J.*, **39**, 689 (1993).

Giddings, J. C., *Dynamics of Chromatography*, Marcel Dekker, New York (1965).

Gladden, L. F., M. P. Hollewand, and P. Alexander, "Characterization of Structural Inhomogeneities in Porous Media," *AIChE J.*, **41**, 894 (1995).

Godbille, E., and P. Devaux, "Use of an 18-mm I.D. Column for Analytical- and Preparative-Scale High-Pressure Liquid Chromatography," *J. Chromatog.*, **122**, 317 (1976).

Guilfoyle, D. N., P. Mansfield, and K. J. Packer, "Fluid Flow Measurement in Porous Media by Echo-Planar Imaging," *J. Magn. Reson.*, **97**, 342 (1992).

Guillot, G., C. Chardaire-Rivière, S. Bobroff, A. Le Roux, J. C. Roussel, and L. Cuiec, "Characterization of Wetting Heterogeneities in Sandstone Rocks by MRI," *Magn. Reson. Imaging*, **12**, 365 (1994).

Guiochon, G., T. Farkas, H. Guan-Sajonz, J.-H. Koh, M. Sarker, B. J. Stanley, and T. Yun, "Consolidation of Particles Beds and Packing of Chromatographic Columns," *J. Chromatog. A*, **762**, 83 (1997).

Guiochon, G., S. G. Shirazi, and A. M. Katti, *Fundamentals of Nonlinear and Preparative Chromatography*, Academic Press, Boston (1994).

Heath, C. A., G. Belfort, B. E. Hammer, S. D. Mirer, and J. M. Pimbley, "Magnetic Resonance Imaging and Modeling of Flow in Hollow-Fiber Bioreactors," *AIChE J.*, **36**, 547 (1990).

Hemminga, M. A., and P. Buurman, eds., "NMR in Soil Science," *Geoderma*, **80** (special issue, 1997).

Hollewand, M. P., and L. F. Gladden, "Transport Heterogeneities in Porous Pellets: II. NMR Imaging Studies Under Transient and Steady-State Conditions," *Chem. Eng. Sci.*, **50**, 327 (1995).

Karger, B. L., L. R. Snyder, and Cs. Horvàth, *An Introduction to Separation Science*, Wiley, New York (1973).

Kärger, J., and W. Heink, "The Propagator Representation of Molecular Transport in Microporous Crystallites," *J. Magn. Reson.*, **51**, 1 (1983).

Knox, J. H., G. R. Laird, and P. A. Raven, "Interaction of Radial and Axial Dispersion in Liquid Chromatography in Relation to the 'Infinite Diameter Effect,'" *J. Chromatog.*, **122**, 129 (1976).

Knox, J. H., and J. F. Parcher, "Effect of Column to Particle Diameter Ratio on the Dispersion of Unsorbed Solutes in Chromatography," *Anal. Chem.*, **41**, 1599 (1969).

La Heij, E. J., P. J. A. M. Kerkhof, K. Kopinga, and L. Pel, "Determining Porosity Profiles During Filtration and Expression of Sewage Sludge by NMR Imaging," *AIChE J.*, **42**, 953 (1996).

Lawing, A. S., L. Lindström, and C. M. Grill, "An Improved Procedure for Packing Annular-Expansion Preparative HPLC Columns," *LC-GC*, **10**, 778 (1992).

Lebon, L., L. Oger, J. Leblond, J. P. Hulin, N. S. Martys, and L. M. Schwartz, "Pulsed Gradient NMR Measurements and Numerical Simulation of Flow Velocity Distribution in Sphere Packings," *Phys. Fluids*, **8**, 293 (1996).

Little, J. N., R. L. Cotter, J. A. Prendergast, and P. D. McDonald, "Preparative Liquid Chromatography Using Radially Compressed Columns," *J. Chromatog.*, **126**, 439 (1976).

Mansfield, P., and P. K. Grannell, "NMR Diffraction in Solids," *J. Phys. C: Solid State Phys.*, **6**, L422 (1973).

Marshall, A. G., and F. R. Verdun, *Fourier Transforms in NMR, Optical and Mass Spectrometry*, Elsevier, Amsterdam (1990).

Martin, H., "Low Peclet Number Particle to Fluid Heat and Mass Transfer in Packed Beds," *Chem. Eng. Sci.*, **33**, 913 (1978).

Neue, U. D., *HPLC Columns*, Wiley-VCH, New York (1997).

Oger, L., C. Gauthier, C. Leroy, J. P. Hulin, and E. Guyon, "Heterogeneities and Characteristic Lengths in Porous Media," *Int. Chem. Eng.*, **32**, 674 (1992).

Rothwell, W. P., and H. J. Vinegar, "Petrophysical Applications of NMR Imaging," *Appl. Optics*, **24**, 3969 (1985).

Sarker, M., and G. Guiochon, "The Packing Stability of Dynamically Compressed Preparative Chromatography Columns," *LC-GC*, **12**, 300 (1994a).

Sarker, M., and G. Guiochon, "Study of the Packing Behavior of Radial Compression Columns for Preparative Chromatography," *J. Chromatog. A*, **683**, 293 (1994b).

Sarker, M., A. M. Katti, and G. Guiochon, "Consolidation of the Packing Material in Chromatographic Columns under Dynamic Axial Compression: II. Consolidation and Breakage of Several Packing Materials," *J. Chromatog. A*, **719**, 275 (1996).

Scheenen, T., D. van Dusschoten, P. A. de Jager, and H. Van As, "Fast Spatially Resolved Displacement Imaging in (Bio)systems," *Proc. Int. Conf. on Magnetic Resonance Microscopy*, Albuquerque, NM (1997).

Seymour, J. D., and P. T. Callaghan, "Generalized Approach to NMR Analysis of Flow and Dispersion in Porous Media," *AIChE J.*, **43**, 2096 (1997).

Stejskal, E. O., and J. E. Tanner, "Spin Diffusion Measurements: Spin Echoes in the Presence of a Time Dependent Field Gradient," *J. Chem. Phys.*, **42**, 288 (1965).

Sternberg, J. C., "Extra-Column Contributions to Chromatographic Band Broadening," *Adv. Chromatog.*, **2**, 205 (1966).

Tallarek, U., K. Albert, E. Bayer, and G. Guiochon, "Measurement of Transverse and Axial Apparent Dispersion Coefficients in Packed Beds," *AIChE J.*, **42**, 3041 (1996).

Tallarek, U., E. Baumeister, K. Albert, E. Bayer, and G. Guiochon, "NMR Imaging of the Chromatographic Process. Migration and Separation of Bands of Gadolinium Chelates," *J. Chromatog. A*, **696**, 1 (1995).

Tallarek, U., D. van Dusschoten, H. Van As, E. Bayer, and G. Guiochon, "Study of Transport Phenomena in Chromatographic Columns by Pulsed Field Gradient NMR," *J. Phys. Chem. B*, **102**, 3486 (1998).

Tessier, J. J., K. J. Packer, J.-F. Thovert, and P. M. Alder, "NMR Measurements and Numerical Simulation of Fluid Transport in Porous Solids," *AIChE J.*, **43**, 1653 (1997).

Train, D., "Transmission of Forces through a Powder Mass During the Process of Pelleting," *Trans. Inst. Chem. Eng. (London)*, **35**, 258 (1957).

Van As, H., W. Palstra, U. Tallarek, and D. van Dusschoten, "Flow and Transport Studies in (Non)consolidated Porous (Bio)systems Consisting of Solid or Porous Beads by PFG-NMR," *Magn. Reson. Imaging*, in press (1998).

van Dusschoten, D., P. A. de Jager, and H. Van As, "Flexible PFG-NMR Desensitized for Susceptibility Artefacts using the PFG Multiple Spin Echo Sequence," *J. Magn. Reson. A*, **112**, 237 (1995).

van Dusschoten, D., C. T. W. Moonen, P. A. de Jager, and H. Van As, "Unravelling Diffusion Constants in Biological Tissue by Combining Carr-Purcell-Meiboom-Gill Imaging and Pulsed Field Gradient NMR," *Magn. Reson. Med.*, **36**, 907 (1996).

Yun, T., and G. Guiochon, "Modeling of Radial Heterogeneity in Chromatographic Columns: II. Separation of a Two-Component Mixture on a Column with Cylindrical Symmetry," *J. Chromatog. A*, **734**, 97 (1996).

Manuscript received Jan. 13, 1998, and revision received June 22, 1998.